

Optical and Near-Infrared Photometric Observation during the Superoutburst of the WZ Sge-Type Dwarf Nova, V455 Andromedae

Risako MATSUI¹, Makoto UEMURA², Akira ARAI¹, Mahito SASADA¹, Takashi OHSUGI²,
Takuya YAMASHITA³, Koji KAWABATA², Yasushi FUKAZAWA¹, Tsumefumi MIZUNO¹,
Hideaki KATAGIRI¹, Hiromitsu TAKAHASHI², Shuji SATO⁴, Masaru KINO⁴, Michitoshi YOSHIDA⁵, Yasuhiro
SHIMIZU⁵, Shogo NAGAYAMA⁵, Kenshi YANAGISAWA⁵, Hiroyuki TODA⁵,
Kiichi OKITA⁵, and Nobuyuki KAWAI⁶

¹*Department of Physical Science, Hiroshima University, Kagamiyama 1-3-1,
Higashi-Hiroshima 739-8526*

²*Astrophysical Science Center, Hiroshima University, Kagamiyama 1-3-1,
Higashi-Hiroshima 739-8526*

³*National Astronomical Observatory of Japan, Osawa 2-21-1,
Mitaka, Tokyo 181-8588, Japan*

⁴*Department of Physics, Nagoya University, Furo-cho, Chikusa-ku, Nagoya 464-8602*

⁵*Okayama Astrophysical Observatory, National Astronomical Observatory of Japan,
Kamogata Okayama 719-0232*

⁶*Department of Physics, Tokyo Institute of Technology, 2-12-1 Ookayama, Meguro-ku, Tokyo 152-8551, Japan*

(Received 2009 March 27; accepted 2009 June 8)

Abstract

We report on optical and infrared photometric observations of a WZ Sge-type dwarf nova, V455 And during a superoutburst in 2007. These observations were performed with the KANATA (V , J , and K_s bands) and MITSuME (g' , Rc , and Ic bands) telescopes. Our 6-band simultaneous observations allowed us to investigate the temporal variation of the temperature and the size of the emitting region associated with the superoutburst and short-term modulations, such as early and ordinary superhumps. A hot (> 11000 K) accretion disk suddenly disappeared when the superoutburst finished, while blackbody emission, probably from the disk, still remained dominant in the optical region with a moderately high temperature (~ 8000 K). This indicates that a substantial amount of gas was stored in the disk even after the outburst. This remnant matter may be a sign of an expected mass-reservoir which can trigger echo outbursts observed in several WZ Sge stars. The color variation associated with superhumps indicates that viscous heating in a superhump source stopped on the way to the superhump maximum, and a subsequent expansion of a low-temperature region made the maximum. The color variation of early superhumps was totally different from that of superhumps: the object was bluest at the early superhump minimum. The temperature of the early superhump light source was lower than that of an underlying component, indicating that the early superhump light source was a vertically expanded low-temperature region at the outermost part of the disk.

Key words: accretion, accretion disk—stars: novae, cataclysmic variables—stars: individual(V455 Andromedae)

1. Introduction

Cataclysmic variables are semi-detached binary systems consisting of a primary white dwarf and a secondary red star. A Roche-lobe-filling red star loses mass through the inner Lagrangian point and the white dwarf accretes. Dwarf novae are a group of cataclysmic variables, showing repetitive outbursts having amplitudes of 2–8 mag (Warner 1995). In the quiescent state of dwarf novae, the optical emission is a superposition of the flux from several components, that is, the thermal emission from the white dwarf and the secondary star, and free-free emission from an optically thin accretion disk and a hot spot where

the gas stream from the secondary hits the disk (Szkody 1976). In an outburst, the thermal emission from an optically thick disk is dominant (Clarke et al. 1984; Horne et al. 1990). SU UMa-type dwarf novae are a subgroup of dwarf novae, exhibiting two types of outburst: a short normal outburst and a long superoutburst. During superoutbursts, their light curves show short-term periodic modulations, called “superhumps”, which have a period that is a few percent longer than the orbital period (Warner 1985).

It is widely accepted that dwarf nova outbursts can be explained by two types of instabilities in the accretion disk (Osaki 1996). The first instability is a thermal insta-

bility (Hōshi 1979). According to the thermal instability model, the accretion disk can take only two thermally stable states. One is a low-viscosity, cool disk consisting of neutral hydrogen gas. The other one is a high-viscosity, hot disk consisting of ionized gas. The disk with partially ionized gas is predicted to be thermally unstable. Dwarf nova outbursts can be interpreted as a state transition from the cool to hot state, which occurs when the disk density reaches a critical value in the cool state.

The second instability is a tidal instability (Whitehurst 1988; Osaki 1989). According to this model, the disk becomes tidally unstable, and deforms to an eccentric disk when the disk radius reaches the 3:1 resonance radius. A strong tidal torque works in an eccentric disk, leading to bright superoutbursts observed in SU UMa stars. An eccentric disk is expected to show prograde precession in the inertial frame of binary systems. The superhump period, slightly longer than the orbital period, can naturally be explained by this precession.

WZ Sge-type dwarf novae form a subclass of SU UMa stars, which only experiences superoutbursts (O’Donoghue et al. 1991; Osaki 1995). They are characterized by quite long (~ 10 yr) intervals of superoutbursts. WZ Sge stars have received attention because they show peculiar variations which are not seen in ordinary SU UMa stars, and whose mechanisms are poorly understood.

WZ Sge stars tend to show echo outbursts after the main superoutburst (Kato et al. 2004). According to the thermal–tidal instability model, the amount of gas in the disk should be minimum just after an superoutburst (Osaki 1989). The long duration of the echo outburst phase and its sudden cessation are, hence, problematic for the disk instability model. Hameury et al. (2000) proposed that an echo outburst is caused by an enhanced mass-transfer rate from the secondary. Patterson et al. (2002) reported that the observation of WZ Sge supported that scenario. On the other hand, Osaki et al. (2001) proposed that an echo outburst can be triggered if the disk viscosity remains high just after the outburst, and the gas is supplied from the outer disk (Kato et al. 1998; Kato et al. 2004). Hellier (2001) suggested that a substantial amount of gas may be stored between the 3:1 resonance and the tidal-limit radius in binary systems having an extreme mass ratio ($M_2/M_1 \lesssim 0.1$), such as WZ Sge-type dwarf novae. Observational evidence for such a mass reservoir for echo outbursts has, however, not been established (Uemura et al. 2008; Kato et al. 2008).

WZ Sge-type dwarf novae exhibit unique short-term periodic modulations only appearing in a very early phase of superoutbursts. They are called “early superhumps”, whose period is in agreement with the orbital period (Patterson et al. 1981; Kato et al. 1996). Since the amplitude of the early superhump depends on the inclination angle of binary systems, it is probably attributed not to the variation due to viscous heating, but to a geometric effect of the accretion disk (Kato 2002). It is proposed that a part of the disk is vertically expanded, and has a non-axisymmetric structure (Kato 2002; Osaki, Meyer 2002; Kunze, Speith 2005).

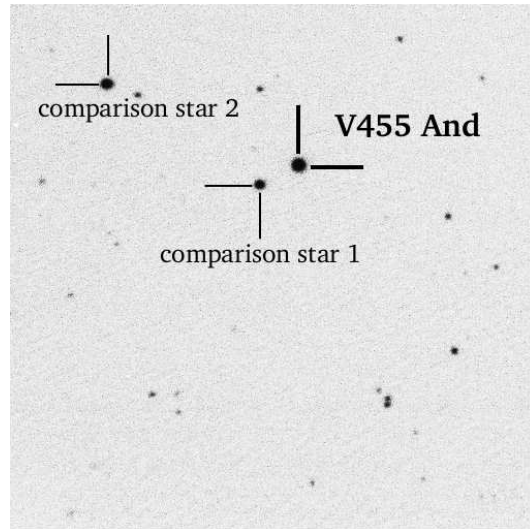


Fig. 1. V-band CCD image of the field of V455 And observed on 15 September 2007 with the KANATA telescope. The field of view is $7' \times 7'$. V455 And and comparison stars are indicated by the black bars.

V455 And was discovered as a dwarf nova candidate from the Hamburg Quasar Survey. Follow-up observations showed an orbital period of 81.09 min and a spectrum similar to that of WZ Sge (Araujo-Betancor et al. 2004; Araujo-Betancor et al. 2005). The first-ever recorded outburst of V455 And was discovered on 2007 September 4¹. As reported in the following section of this paper, V455 And was actually confirmed to be one of the WZ Sge stars from observations during the outburst. The object became a very bright source, reaching the 8th magnitude in the V band at maximum. It, hence, provided a great chance to study WZ Sge phenomena in detail. We performed optical–near-infrared multi-band photometric observations in order to provide the color variation associated with a superoutburst as well as early and ordinary superhumps. In this paper, we report on the results of our observation. We, furthermore, investigate the temporal variation of the temperature and the size of the emitting region of the disk using the multi-band data. In section 2, the observation and image reduction are described. Our observational results are shown in section 3. The implication of the results is discussed in section 4. Finally, we summarize our findings in section 5.

2. Observations

We performed photometric observations at two sites. First, observations at Higashi-Hiroshima Observatory were carried out with the 1.5-m KANATA telescope. We used the instrument “TRISPEC (Triple Range Imager and SPECTrometer with Polarimetry)” attached to the Cassegrain focus of the telescope (Watanabe et al. 2005). Photometric observations were performed simultaneously

¹ <http://ooruri.kusastro.kyoto-u.ac.jp/pipermail/vsnet-alert/2007-September/001152.html>

Table 3. Magnitude of the comparison stars

filter	mag (comp.1)	mag (comp.2)
g'	13.17 ± 0.01	12.45 ± 0.01
V	12.70 ± 0.01	12.20 ± 0.01
Rc	12.12 ± 0.01	11.85 ± 0.01
Ic	11.63 ± 0.01	11.50 ± 0.02
J	10.89 ± 0.02	11.05 ± 0.02
K_s	10.26 ± 0.02	10.71 ± 0.02

in the V , J , and K_s bands. The exposure times of V , J , and K_s -band observations were 10 or 30, 2 or 5, and 1 s, respectively, depending on the sky condition. An example of the V -band images is shown in figure 1. Second, the observations at Okayama Astrophysical Observatory were carried out with the 50-cm MITSuME telescope. The observations were performed simultaneously in the g' , Rc , and Ic bands. The exposure times of the three bands were between 5 and 60s. The journal of the observations is given in tables 1 and 2 for the Higashi-Hiroshima and Okayama observatories, respectively.

After dark subtraction and flat fielding, we performed aperture photometry, and obtained differential magnitudes of the object relative to the comparison stars. The comparison stars that we used are indicated in figure 1. Comparison stars 1 and 2 are located at $RA = 23^h34^m04.^s19$, $DEC = +39^\circ21'24''.1$, and $RA = 23^h34^m15.^s09$, $DEC = +39^\circ22'47''.4$, respectively. The optical and near-infrared magnitudes of the comparison stars were quoted from Henden (2006)² and the 2MASS catalog (Skrutskie et al. 2006), respectively. The magnitude of the comparison star in the g' band was converted from the B and V magnitudes with the following formula (Smith et al. 2002):

$$g' = V + 0.54(B - V) - 0.07.$$

The magnitudes of the comparison stars are listed in table 3.

The constancy of the magnitude of comparison star 1 was checked with comparison star 2. No significant variation was seen over ~ 0.04 mag in the relative magnitude between comparison stars 1 and 2 throughout our observation. In the following sections, we show the results using comparison star 1. We confirmed that the magnitudes calculated with comparison star 2 are in agreement with those with comparison star 1 within the errors in all bands. The magnitude errors of the comparison star were included in those of the object in the following analysis for the spectral energy distribution (SED).

The interstellar extinction in the direction of V455 And is estimated to be small, $A_V = 0.34$, according to the database of Schlegel et al. (1998). This can be considered as being an upper-limit of the extinction in V455 And. The actual extinction is probably significantly smaller than the upper-limit, since V455 And is a nearby source; the distance is estimated to be 90 ± 15 pc (Araujo-Betancor

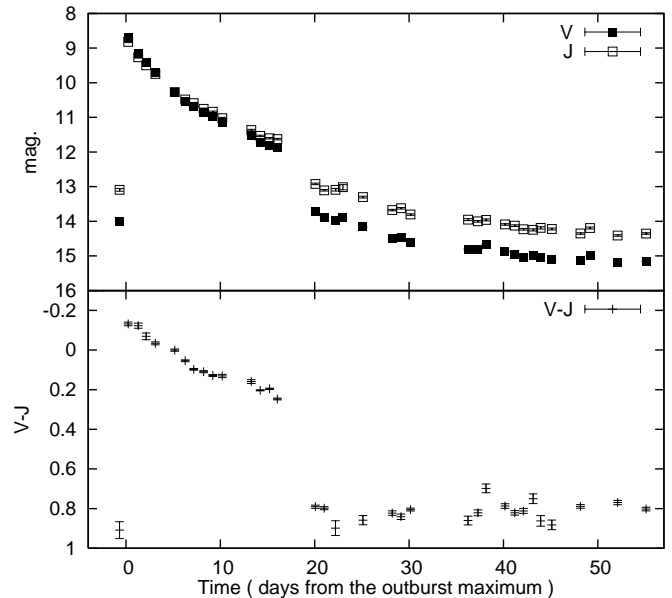


Fig. 2. Light curve and color variation during the outburst. The upper panel shows the light curves in the V and J bands represented by the filled and open squares, respectively. The lower panel shows the color variation of $V - J$. The figure includes observations for ~ 2 months, from 4 September to 30 October 2007. The abscissa is the elapsed days from the outburst maximum (5.5 September 2007(UT) [JD 2454349.0]). Errors of the photometric points are also shown, but they are smaller than the symbol size.

et al. 2005). It is difficult to perform an accurate correction of the extinction with our available data. In this paper, we neglect the interstellar extinction.

3. Result

3.1. The 2007 Outburst of V455 And

Figure 2 illustrates the overall light curve and color variation of V455 And during the 2007 outburst. The outburst of V455 And was discovered on 4 September 2007. We started to observe the object just after its discovery. The object was rapidly rising with -5.8 magday $^{-1}$ in the V band during our first night observation on 4 September. On the next day, 5 September, the outburst reached the maximum when the magnitude was 8.69 ± 0.01 in the V band. Hereafter, we denote the time as T , the elapsed days from the outburst maximum, defining $T = 0.0$ as 5.5 September 2007(UT) (JD 2454349.0).

After the object reached the maximum, it had declined from $V = 8.7$ to 11.9 for 17 d. The fading rate was calculated to be 0.31 ± 0.02 magday $^{-1}$ in the V band at $T = 0-5$. It, then, significantly decreased to 0.13 ± 0.01 magday $^{-1}$ at $T = 9-15$. A change of the fading rate occurred at $T \sim 6$. Such a feature is commonly observed in WZ Sge-type dwarf novae (Kato et al. 2001). The outburst continued at least until $T \sim 17$, and then a rapid fading from the outburst was observed at $T = 20$. The rapid fading

² <ftp://ftp.aavso.org/public/calib/hs2331.dat>

Table 1. Observation log for the KANATA telescope

T (days)	Time [+JD2454000]	<i>V</i> mag*	<i>J</i> mag*	<i>K_s</i> mag*	Frames
-0.7027—0.6539	48.2973—48.3461	14.00±0.03	13.09±0.04	12.64±0.05	34
0.1167—0.3215	49.1167—49.3215	8.69±0.01	8.82±0.02	8.59±0.02	307
1.2300—1.3142	50.2300—50.3142	9.14±0.02	9.27±0.02	8.97±0.02	77
2.1005—2.2405	51.1005—51.2405	9.43±0.02	9.50±0.03	9.33±0.04	89
3.0409—3.1868	52.0409—52.1868	9.71±0.01	9.75±0.02	9.51±0.02	352
5.1006—5.2510	54.1006—54.2510	10.27±0.01	10.27±0.02	10.06±0.02	400
6.2552—6.3128	55.2552—55.3128	10.54±0.01	10.48±0.02	10.27±0.02	170
7.1196—7.2517	56.1196—56.2517	10.68±0.01	10.59±0.02	10.35±0.02	374
8.2005—8.2681	57.2005—57.2681	10.86±0.01	10.75±0.02	10.51±0.02	199
9.0606—9.3089	58.0606—58.3089	10.97±0.01	10.84±0.02	10.59±0.02	360
10.0668—10.2980	59.0668—59.2980	11.15±0.01	11.02±0.02	10.77±0.03	194
13.2629—13.3016	62.2629—62.3016	11.52±0.01	11.37±0.02	11.18±0.04	81
14.1349—14.3122	63.1349—63.3122	11.74±0.01	11.53±0.02	11.29±0.02	1048
15.1447—15.9998	64.1447—64.9998	11.80±0.01	11.60±0.02	11.34±0.02	790
16.0002—16.1419	65.0002—65.1419	11.88±0.01	11.63±0.02	11.35±0.03	466
16.1350—16.1456	65.1350—65.1456	12.74±0.02	—	—	18
21.0208—21.0517	69.0208—60.0517	13.90±0.01	13.11±0.02	12.32±0.03	588
22.1129—22.2611	71.1129—71.2611	13.99±0.02	13.09±0.04	12.43±0.08	62
22.9737—22.9970	71.9737—71.9970	13.90±0.02	13.02±0.08	12.39±0.11	27
24.9586—25.3170	73.9586—74.3170	14.16±0.02	13.30±0.03	12.54±0.04	127
28.1306—28.3176	77.1306—77.3176	14.50±0.01	13.68±0.02	12.87±0.03	210
29.0899—29.2791	78.0899—78.2791	14.47±0.02	13.62±0.02	12.83±0.03	173
30.0781—30.2068	79.0781—79.2068	14.61±0.01	13.80±0.02	13.05±0.03	200
31.1622—31.1672	80.1622—80.1672	14.59±0.02	13.77±0.04	13.07±0.22	8
36.1646—36.2881	85.1646—85.2881	14.81±0.02	13.95±0.03	13.18±0.03	111
37.0321—37.3320	86.0321—86.3320	14.82±0.02	14.00±0.02	13.10±0.05	84
38.1215—38.1827	87.1215—87.1827	14.66±0.01	13.96±0.03	12.96±0.06	94
40.1162—40.2183	89.1162—89.2183	14.88±0.01	14.09±0.02	13.23±0.03	170
41.1390—41.2589	90.1390—90.2589	14.95±0.01	14.13±0.02	13.27±0.03	195
42.0535—42.1757	91.0535—91.1757	15.04±0.01	14.23±0.02	13.35±0.03	145
42.9389—43.2362	91.9389—92.2362	15.00±0.02	14.25±0.03	13.26±0.05	94
43.9468—43.9531	92.9468—92.9531	15.05±0.02	14.19±0.03	13.35±0.04	10
45.1280—45.1338	94.1280—94.1338	15.10±0.02	14.22±0.03	13.41±0.06	10
46.9391—46.9449	95.9391—95.9449	15.13±0.03	14.43±0.08	12.88±0.12	9
48.0630—48.2188	97.0630—97.2188	15.14±0.01	14.35±0.02	13.46±0.03	210
49.1694—49.1754	98.1694—98.1754	14.99±0.02	14.19±0.03	13.64±0.05	10
52.0617—52.1322	101.0617—101.1322	15.18±0.01	14.41±0.02	13.44±0.04	103
55.0422—55.1755	104.0422—104.1755	15.16±0.01	14.35±0.02	13.45±0.03	200

*Magnitudes are averaged ones in each run.

Table 2. Observation log for the MITSuME telescope

T (days)	Time [+JD2454000]	g' mag*	Rc mag*	Ic mag*	Frames
1.9503—2.3055	50.9503—51.3055	9.33±0.01	9.27±0.01	9.28±0.01	1193
5.0391—5.3237	54.0391—54.3237	10.30±0.01	10.23±0.01	10.19±0.01	2591
7.0299—7.3262	56.0299—56.3262	10.71±0.01	10.61±0.01	10.55±0.01	2700
7.9553—8.2677	56.9553—57.2677	10.91±0.01	10.79±0.01	10.73±0.01	1748
8.9281—9.1159	57.9281—58.1159	11.01±0.01	10.91±0.01	10.83±0.01	863
12.0480—12.3326	61.0480—61.3326	11.34±0.01	11.25±0.01	11.17±0.01	683
12.9244—13.1539	61.9244—62.1539	11.50±0.01	11.40±0.01	11.31±0.01	1215
13.9231—14.3270	62.9231—63.3270	11.77±0.01	11.66±0.01	—	2214
15.9210—16.3274	64.9210—65.3274	11.94±0.01	11.82±0.01	11.70±0.01	1109
17.1428—17.2706	66.1428—66.2706	12.13±0.01	11.97±0.01	11.84±0.01	543
19.9168—20.1476	68.9168—69.1476	13.83±0.01	13.43±0.01	13.20±0.01	983
20.9478—21.3074	69.9478—70.3074	14.07±0.01	13.65±0.01	13.42±0.01	1480
21.9398—22.2135	70.9398—71.2135	14.10±0.01	13.68±0.01	13.45±0.01	1061
27.9092—28.3009	76.9092—77.3009	14.61±0.01	14.26±0.01	14.02±0.01	709
29.9078—30.3033	78.9078—79.3033	14.68±0.01	14.34±0.01	14.12±0.01	831
30.9148—31.2400	79.9148—80.2400	14.70±0.01	14.35±0.01	14.13±0.01	704
34.9301—35.0705	83.9301—84.0705	14.88±0.01	14.51±0.01	14.31±0.01	140
38.0765—38.2248	87.0765—87.2248	14.81±0.01	14.43±0.01	14.22±0.01	224
38.8993—39.1974	87.8993—88.1974	14.90±0.01	14.54±0.01	14.33±0.01	422
39.8981—40.2558	88.8981—89.2558	14.99±0.01	14.66±0.01	14.45±0.01	565
40.8971—41.2447	89.8971—90.2447	15.03±0.01	14.70±0.01	14.50±0.01	510
41.8968—42.2413	90.8968—91.2413	15.12±0.01	14.78±0.01	14.60±0.01	377
42.8957—42.9852	91.8957—91.9852	15.06±0.02	14.71±0.01	14.53±0.02	87
43.8952—44.2343	92.8952—93.2343	15.15±0.01	14.80±0.01	14.61±0.01	352
44.9451—45.2134	93.9451—94.2134	15.16±0.01	14.82±0.01	14.62±0.01	299
45.9946—46.2070	94.9946—95.2070	15.21±0.01	14.88±0.01	14.70±0.01	226
46.8927—46.9790	95.8927—95.9790	15.22±0.02	14.86±0.01	14.69±0.02	99
47.9333—48.1951	96.9333—97.1951	15.21±0.01	14.85±0.01	14.68±0.01	161
48.8905—49.1993	97.8905—98.1993	15.22±0.01	14.87±0.01	14.69±0.01	351
52.0067—52.1898	101.0067—101.1898	15.24±0.01	14.88±0.01	14.71±0.01	152
52.8876—53.0824	101.8876—102.0824	15.20±0.01	14.84±0.01	14.67±0.01	208
55.0617—55.1856	104.0617—104.1856	15.23±0.01	14.89±0.01	14.70±0.01	141

*Magnitudes are averaged ones in each run.

stopped at 2.7 mag brighter than the quiescence in the V band. Then, the object again started gradual fading. Those temporal behaviors are common to the light curves of the other wave-bands, that is, the g' , Rc , Ic , and K_s bands. V455 And exhibited no echo outburst, which has been observed in several WZ Sge stars (Kato et al. 2004).

The color index took a minimum value of $V - J = -0.13 \pm 0.01$ when the brightness was at the maximum. The color index gradually increased with time during the outburst. As can be seen in the lower panel of figure 2, the color curve also shows a break at $T \sim 6$. The color suddenly changed to be red, $V - J \sim 0.8$, at the same time as when the outburst finished. After the outburst, the color remained almost constant at ~ 0.8 , while the brightness continued a gradual decline. Thus, the brightness—color relation in outburst was different from that after the outburst. This result suggests that a dominant radiation mechanism or component changed when the outburst finished.

3.2. SED Variation during the Outburst

Using 6-band photometric observations, we investigated the radiation mechanism, the size, and the temperature of the emitting region during and after the outburst. Figure 3 shows the SEDs of the optical–infrared region. The top, middle, and bottom panels show the SED at $T = 5, 13,$ and 22 , respectively.

We need to develop an SED model to obtain physical parameters of the emitting region for both the outburst and post-outburst states. It is considered that the thermal emission from the optically thick disk is dominant in the optical range during dwarf nova outbursts (Clarke et al. 1984; Horne et al. 1990). It has been proposed, however, that WZ Sge stars have more complex emission-components and structure of the accretion disk (Smak 1993; Nogami et al. 2009). In the post-outburst and quiescent states, furthermore, it has been believed that several components can contribute to the optical–near-infrared emission, for example, the white dwarf, the optically thick/thin disk, the hot spot, and the secondary star.

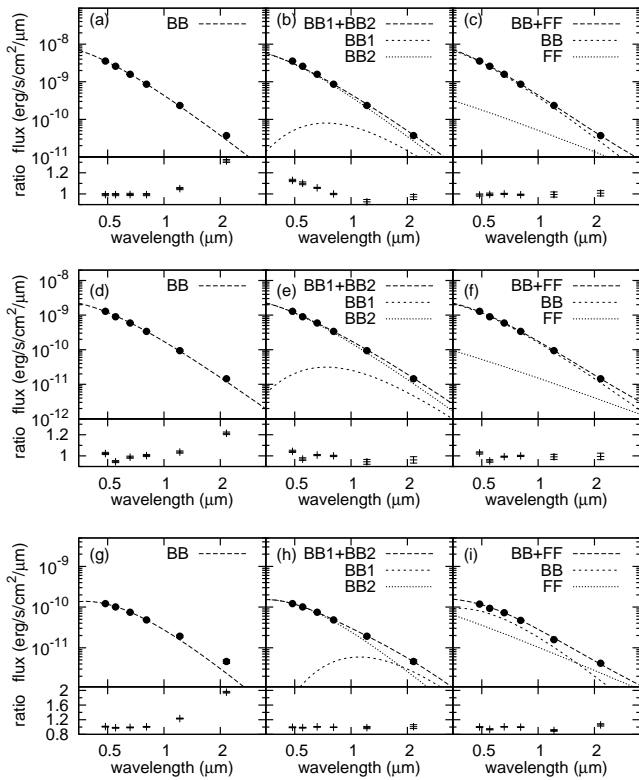


Fig. 3. Observed SEDs and best models. The filled circles indicate the observed fluxes in the g' , V , Rc , Ic , J , and K_s bands. Panels (a), (b), and (c) show the SEDs at $T = 5$ when early superhumps appeared. Panels (d), (e), and (f) show those at $T = 13$ when superhump appeared. Panels (g), (h), and (i) show those at $T = 22$, after the outburst. The model SEDs in the left, middle, and right panels are a blackbody radiation, two blackbody components, and the combination model of blackbody and a 10^5 K free-free emissions, respectively. In the middle and right panels, we show each emission as well as the total model SEDs. Lower frame of each panel shows the ratio of the observed SED to the model. Errors of each point are shown in the figure, but most of them are smaller than the size of the symbols.

Araujo-Betancor et al. (2005) reported that no sign of the secondary star was detected at quiescence in V455 And. The contribution from the secondary star is, hence, negligible in the SED of V455 And, while the other components are possibly significant.

On the other hand, the “spectral” resolution of our 6-band photometric data is evidently too low to resolve the individual components. Our analysis, hence, focused not on the detailed structure of the emission components, but on the most dominant source in the optical–near-infrared regime. As reported in subsection 3.3, early and ordinary superhumps were observed in all wave-bands during the outburst of V455 And, which indicates that the optically thick disk is a dominant source, as in ordinary SU UMa stars. We, hence, tried to fit the SEDs with a blackbody radiation component. The best-fitted models are indicated by the dashed lines in panels (a), (d), and (g) in

figure 3. The SEDs are well reproduced by the blackbody radiation in the short wavelength range from the g' to Ic band, as can be seen in the panels. On the other hand, there is an excess over the blackbody emission in the K_s -band. Thus, another emission was dominant in the K_s band in addition to the blackbody radiation, which was dominant on the blue side.

In order to reproduce the K_s -band excess, we attempted to fit the SEDs using two types of additional components. The first one was low-temperature blackbody emission. The obtained best-fitted models are indicated with the dashed line in panels (b), (e), and (h) in figure 3. The second model is free-free emission. In dwarf novae at quiescence, the free-free emission accounts for $\sim 50\%$ of the optical flux (Szkody 1976). Its temperature has been estimated to be $(0.5-1) \times 10^5$ K. It probably originates from a hot spot or optically thin disk. Even in outburst, we can expect a contribution of the free-free emission from the optically thin area in the accretion disk. The contribution can be large in edge-on systems, such as V455 And (Araujo-Betancor et al. 2005), because the optically thin area above the optically thick disk is apparently large. We tried to fit the SED with a combination model with blackbody and free-free emission. The temperature of the free-free emission could not, however, be significantly determined because the dependency of the spectral slope is quite low in the optical region in the case of a temperature of $\gtrsim 10^4$ K. The excess over the blackbody emission is, furthermore, too small even in the near-infrared region to significantly constrain the temperature of the free-free emission. Consequently, we fixed the temperature of the free-free emission as 10^5 K in all cases. The best-fitted models are indicated by the dashed lines in panels (c), (f), and (i) in figure 3. Although the models in the middle and the right panels are different, both models well reproduce the observed SEDs. It is difficult to determine the SED model with only our available data. In this paper, we draw no conclusion about the emission mechanism of the K_s -band excess.

Table 4 gives the temperature of the blackbody emissions obtained with the three SED models. The first column gives the time in T . The second column gives the temperature from the single blackbody model. The third and fourth columns give the temperatures from the two blackbody model. The fifth column gives the blackbody temperature from the combination model of blackbody and free-free emission. It is preferable that the additional component for the K_s -band excess has little influence on the high-temperature blackbody component, because the observed SEDs are almost reproduced by it. As can be seen from table 4, the temperature makes a sudden jump at $T = 13$ in the two-blackbody model, which is less likely to indicate a real variation. It should also be noted that the low-temperature blackbody component has an atypically high temperature only at $T = 2$. On the other hand, the blackbody temperature from the blackbody+free-free model shows a similar variation to that from the single blackbody model. These results indicate that the blackbody+free-free model is more suitable for our anal-

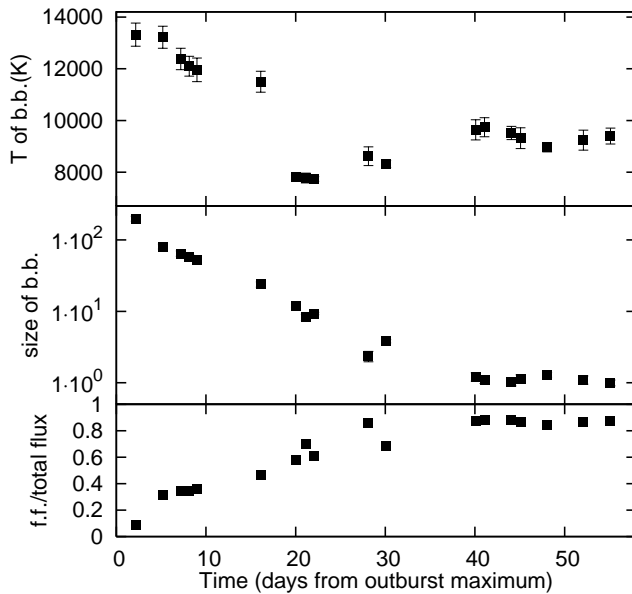


Fig. 4. Temporal variation of the blackbody temperature (top), size (middle), and the ratio of the flux density of the free-free emission to the total flux at $2.16\mu\text{m}$. (bottom). These parameters were estimated with the combination model of a blackbody and free-free emission. The abscissa shows the time in T . The emitting size of the blackbody emission was normalized by the value on $T = 55$. Errors are mostly smaller than the symbol size.

ysis. Hereafter, we use the blackbody+free-free model to describe the observed SED. As mentioned above, it does not mean that we conclude the nature of the K_s -band excess to be free-free emission. The intensity of the free-free emission can be regarded to be just an indicator of the degree of the K_s -band excess.

Figure 4 shows the temporal variation of the best-fitted parameters of the combination model of blackbody and 10^5 K free-free emission. The temperature of the blackbody radiation gradually decreases during the outburst ($T = 0$ –19). When the outburst finishes, the temperature rapidly declines to ~ 8000 K. It again slightly increases from $T \sim 30$. It reaches ~ 10000 K at $T \sim 40$. After that, it remains constant. In contrast to the temperature variation, the emitting size of the blackbody component gradually decreases during, and even after, the outburst for $T = 0$ –40. No dramatic change is seen when the outburst finishes, as can be seen in the temperature variation.

As shown in the bottom panels of figure 3, we found that the blackbody radiation was still strong on the blue side even after the outburst. According to the disk instability model, the emission from the optically thick disk should significantly decrease after the outburst. It is, hence, not trivial that the blackbody component just after the outburst originated from the disk. The disk is, however, still an optimal candidate, because the temperature of ~ 8000 K is significantly lower than the white-dwarf temperature in V455 And (Araujo-Betancor et al. 2005)

and much higher than the secondary-star temperature. Our result, thus, indicates that a hot optically thick accretion disk disappeared when the outburst finished, while the disk still remained optically thick with a moderately high temperature for 10–20 d, even after the outburst. The decline of the size stopped at $T \sim 40$, and subsequently remained constant. The observed color index of $V - J$ was constant after the outburst, because $V - J$ of the ~ 8000 K blackbody emission was similar to that of the free-free one.

As shown in the bottom panel of figure 4, the contribution of the free-free emission at $2.16\mu\text{m}$ (or the degree of the K_s -band excess) was small at the maximum of the outburst. It, then, gradually increased between $T = 0$ –40. It became dominant after the outburst. After $T \sim 40$, it was almost constant at a fraction of the total flux of about 0.85.

3.3. Short-Term Variation Observed in V455 And

V455 And showed short-term variations during the outburst. We report observational features of them in this section.

Figure 5 shows the light curves at $T = 3$ and 5. Clear short-term variations were detected with amplitudes of ~ 0.4 mag on both days. Their profile consists of rapid variations with a timescale of ~ 50 s superimposed on double-peaked periodic modulations (more clearly seen in the phase-averaged light curves in figure 7). The double-peaked feature is reminiscent of early superhumps observed in WZ Sge-type dwarf nova.

Maehara et al. (2007)³ confirmed that those modulations were actually early superhumps based on their period analysis, which showed that the period was in agreement with the orbital period of V455 And. Kato et al. (2007)⁴ reported the period of the early superhump to be 0.056267 ± 0.000002 d.

Figure 6 shows the short-term variations at $T = 12$ and 14. In these cases, short-term variations had a single peak profile with amplitudes of ~ 0.2 mag (also see figure 8). As in figure 5, rapid variations were still seen particularly at $T = 12$. Their features are consistent with those of superhumps observed in SU UMa-type dwarf novae. Kato et al. (2007)⁵ confirmed that those modulations were actually superhumps based on their period analysis, which showed that the period was longer than the orbital period of V455 And. Maehara et al. (2007)⁶ reported the superhump period to be 0.057093 ± 0.000015 d. It is 1.39% longer than the orbital period of V455 And.

Those detections of the early and ordinary superhumps established the WZ Sge-type nature of V455 And. The outburst in 2007 was, hence, actually a superoutburst of

³ <http://ooruri.kusastro.kyoto-u.ac.jp/pipermail/vsnet-alert/2007-September/001170.html>

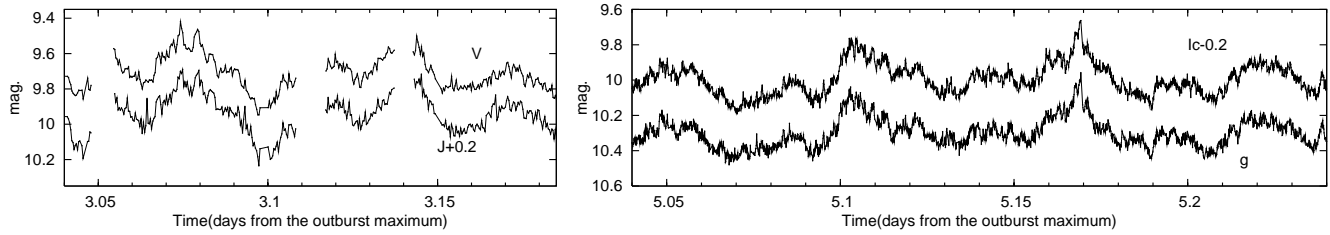
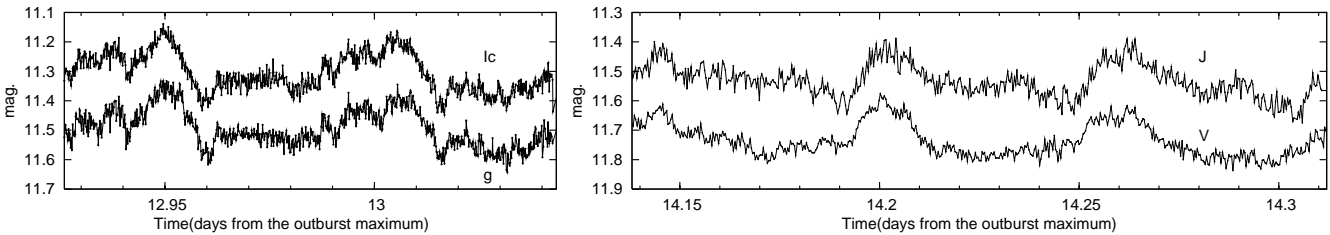
⁴ <http://ooruri.kusastro.kyoto-u.ac.jp/pipermail/vsnet-alert/2007-September/001185.html>

⁵ <http://ooruri.kusastro.kyoto-u.ac.jp/pipermail/vsnet-alert/2007-September/001204.html>

⁶ <http://ooruri.kusastro.kyoto-u.ac.jp/pipermail/vsnet-alert/2007-September/001222.html>

Table 4. Temperature of the blackbody emission in the three models.

T (days)	Single blackbody model	Two-blackbody model		Blackbody+free-free model
	Temp. (K)	Temp.1 (K)	Temp.2 (K)	Temp. (K)
2.16024	13090 \pm 540	14600 \pm 180	5840 \pm 140	13440 \pm 370
5.18139	12560 \pm 380	14510 \pm 140	3850 \pm 70	13300 \pm 330
7.17812	11730 \pm 320	13410 \pm 120	3700 \pm 70	12360 \pm 340
8.13689	11550 \pm 310	13140 \pm 120	3650 \pm 70	12200 \pm 180
9.00140	11510 \pm 370	13040 \pm 220	3650 \pm 70	12080 \pm 160
13.0172	11110 \pm 370	14000 \pm 1060	5260 \pm 500	11320 \pm 200
16.1102	10760 \pm 290	12710 \pm 800	3670 \pm 300	11500 \pm 400
20.0287	7700 \pm 170	8280 \pm 60	2890 \pm 50	7800 \pm 90
21.1294	7670 \pm 140	8280 \pm 90	2630 \pm 60	7780 \pm 190
22.0726	7620 \pm 170	8210 \pm 70	2770 \pm 50	7740 \pm 90
28.1200	7890 \pm 170	8900 \pm 320	2570 \pm 120	8620 \pm 360
30.1101	7960 \pm 180	8820 \pm 220	2560 \pm 110	8320 \pm 130
40.0859	8180 \pm 200	8620 \pm 60	2700 \pm 20	9640 \pm 390
41.0600	8250 \pm 200	9200 \pm 140	2470 \pm 50	9740 \pm 370
44.0659	8280 \pm 210	9140 \pm 80	2440 \pm 50	9520 \pm 260
45.0812	8150 \pm 200	9080 \pm 210	2510 \pm 70	9320 \pm 400
48.0548	8100 \pm 190	9120 \pm 60	2500 \pm 10	8960 \pm 170
52.0996	8110 \pm 190	8970 \pm 60	2440 \pm 50	9240 \pm 390
55.1236	8200 \pm 210	8970 \pm 60	2360 \pm 20	9400 \pm 310

**Fig. 5.** Light curves of early superhumps at $T = 3$ and 5 . The abscissa and ordinate denote the time in T and mag, respectively. The left panel shows the light curves at $T = 3$ in V and $J(+0.2)$ mag. The right panel shows those at $T = 5$ in g' and $Ic(-0.2)$ mag.**Fig. 6.** Light curves of superhumps at $T = 12$ and 14 . The abscissa and ordinate denote the time in T and magnitude, respectively. The left panel shows the light curves at $T = 12$ in Ic and g' mag. The right panel shows those at $T = 14$ in V and J mag.

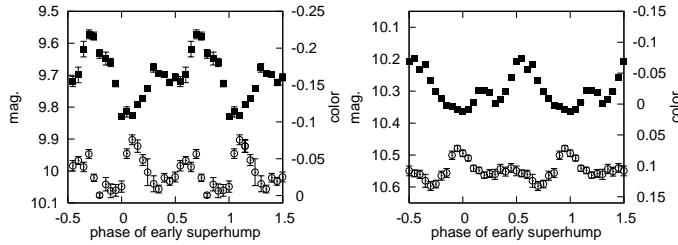


Fig. 7. Phase-averaged light curves and color variations of early superhumps. In the left panel, the filled squares and open circles represent the V -band mag and the $V - J$ color at $T = 3$, respectively. In the right panel, they represent the g' -band mag and $g - Ic$ color at $T = 5$. The abscissa represents the phase of an early superhump, and its origin shows the phase of the early superhump minimum.

WZ Sge-type dwarf novae. We detected typical early superhumps from $T = 0$ to 6. Photometric studies show that the superhump appeared from $T = 7$ and the early superhump completely disappeared on $T = 8$ (Maehara, H. in private communication).

3.4. Color and SED Variation Associated with Early and Ordinary Superhumps

Our multicolor photometry allowed us to investigate the color and SED variations associated with early and ordinary superhumps. In order to see small color variations, we analyzed phase-averaged light curves of them for each night.

Figure 7 shows the phase-averaged light curve and the color variations of early superhumps. In the left panel, the filled squares and open circles represent the V -band mag and $V - J$ color at $T = 3$, respectively. In the right panel, they represent the g' -band mag and $g - Ic$ color at $T = 5$. The observed light curves were folded with an early superhump period of 0.056267 ± 0.000002 d, reported in Kato et al. (2007)⁷. This is the first time that the color variation was successfully observed in early superhumps. The object was the bluest at the early superhump minimum. This indicates that the temperature of the early superhump light source was lower than that of an underlying component. The object became reddest during the fading phase from the maximum to the minimum of early superhumps. Those features were commonly seen at $T = 3$ and 5.

Figure 8 is the same as figure 7, but for ordinary superhumps. The left and right panels represent the observations at $T = 10$ and 14, respectively. The observed light curves were folded with a superhump period of 0.057093 ± 0.000015 d (Maehara et al. 2007)⁸. The object was reddest at the superhump minimum. As the brightness increased, the color became bluer. The object became

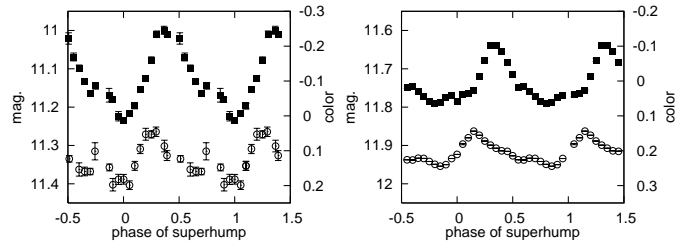


Fig. 8. Phase-averaged light curves and color variations of superhumps. The left and right panels represent the observations at $T = 10$ and 14, respectively. The filled squares and open circles represent V -band mag and $V - J$ color, respectively. The abscissa represents the phase of superhump, and its origin shows the phase of the superhump minimum.

bluest before the superhump maximum. Thus, the color behaviors were different from that of early superhumps; the hump component was red in the early superhump, while it was blue in the ordinary superhump.

In order to study the temperature variation of the superhump light source from our data, we should know the structure of emitting sources. Early and ordinary superhump light sources have been considered to be located at an outer part of the accretion disk (Warner, O'Donoghue 1988; Osaki, Meyer 2002; Kato 2002). The inner part of the disk, on the other hand, probably remains non-variable even during the humps. The observed flux can, hence, be a superposition of the light from the hump component in the outer disk and the non-variable component in the inner disk. It might be better that we use an SED model including both the hump and non-variable components. As mentioned in subsection 3.2, on the other hand, it is difficult for our data to resolve both components without any assumptions. In this section, we present an analysis using a simple model, the same as in subsection 3.2: the blackbody and the 10^5 K free-free emission model. In other words, we regard the hump source as an entire disk in this section. We also performed an analysis using the model with both components, while the results depended on several assumptions for the non-variable component. It is presented in subsection 4.1.

The analysis of SED required simultaneous 6-band photometric data with high quality through a few hours of one night. We had four-night data at $T = 5, 7, 8,$ and 14 which could be used for our SED analysis.

Figure 9 shows the temporal variation of the parameters of our SED model associated with early and ordinary superhumps. The top panels show the observed V -band light curves. The middle and bottom panels show the estimated temperature and the size of the blackbody emission region, respectively. Panels (a), (b), (c), and (d) represent the results at $T = 5, 7, 8,$ and 14, respectively.

Figure 9a shows the result for the early superhump. At the early superhump minimum (phase ~ 0.00), the temperature was highest and the emitting size was smallest. The light curve correlates well with the emitting size. This

⁷ (<http://ooruri.kusastro.kyoto-u.ac.jp/pipermail/vsnet-alert/2007-September/001185.html>)

⁸ (<http://ooruri.kusastro.kyoto-u.ac.jp/pipermail/vsnet-alert/2007-September/001222.html>)

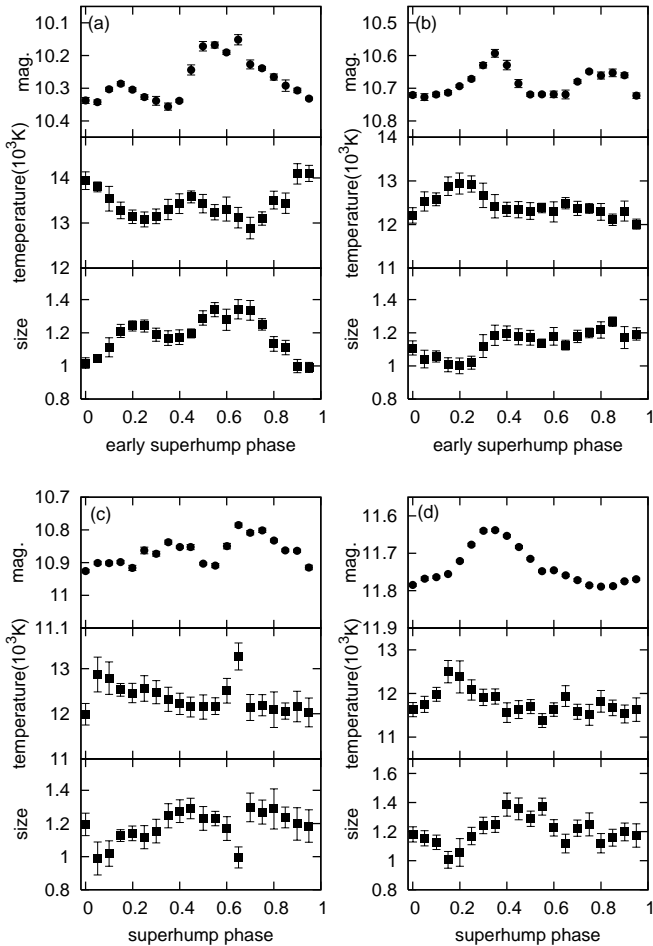


Fig. 9. Temporal variation of the best-fitted parameters of the blackbody emission associated with early and ordinary superhumps. The top panels show the observed V -band light curves. The middle and bottom panels show the estimated temperature and the size of blackbody emission region, respectively. The emitting size was normalized at the phase of the minimum. The abscissa represents the phase of the humps. Panels (a), (b), (c), and (d) represent the results at $T = 5, 7, 8,$ and 14 , respectively.

suggests that the nature of early superhumps is the apparent expansion of a low temperature region.

Figure 9d shows the result for the ordinary superhump. From the superhump minimum (phase ~ 0.00), the temperature and the brightness increase, while the emitting size decreases. The temperature maximum precedes the superhump, and the superhump reaches maximum after the temperature starts to decline. After the superhump maximum, the object fades, first by a decrease in the temperature, and then by a decrease of the size.

The accretion disk is believed to be deformed to a precessing eccentric disk when superhumps are observed. Due to the orbital motion of the secondary star, the eccentric disk is periodically heated by a strong tidal torque, making superhumps. The early phase of the superhump (phase $\sim 0.00 - 0.15$) in figure 9d probably corresponds to the phase that the disk temperature increased due to a viscous heating effect. After the heating stopped, the object entered an expansion-cooling phase. It was probably an outward expansion of the disk as a result of angular-momentum transported from the heated area.

Figure 9b and 9c show short-term modulations during the transition phase from the early to ordinary superhump phase. They have small amplitudes and double-peaked profiles. We can see a hint of two cycles of the heating and expansion-cooling process associated with the primary and secondary maximum in those panels. Their behavior is not similar to that of the early superhump, but rather is similar to that of the ordinary superhump. The early superhump signal may have already been quite weak at $T = 7$ and 8 .

Figure 10 shows the temporal variation of the emitting size against the temperature of the blackbody emission. Panels (a), (b), (c), and (d) represent the results on $T = 5, 7, 8,$ and 14 , respectively. Panel (a) shows the result for the early superhump. First (phase 0.00), the temperature is high, and then gradually declines as the emission size increase. Both the emitting size and the temperature increase in phase ~ 0.40 . We note that heating-expanding feature is only seen in panel (a). After phase 0.70 in panel (a), the object returns to the point of phase 0.00 on a similar track to phase 0.00–0.30. In the case of the superhump shown in panel (d), the disk is first heated and shrunk. After the temperature reaches the maximum, the object starts rapid cooling and expansion until phase 0.35. This “V”-shaped track suggests a process with viscous heating and cooling by expansion. Such a “V”-shaped pattern is not seen in the track of early superhumps. In panels (b) and (c), two cycles of the heating and cooling process are indicated by the two “V”-shaped patterns around phase 0.20 and 0.65 in panel (b) and phase 0.05 and 0.65 in panel (c).

4. Discussion

4.1. Contribution of the Non-Variable Component from an Inner Part of the Accretion Disk

In subsection 3.4, we analyzed the SEDs, while assuming that the hump component is the entire disk. We also

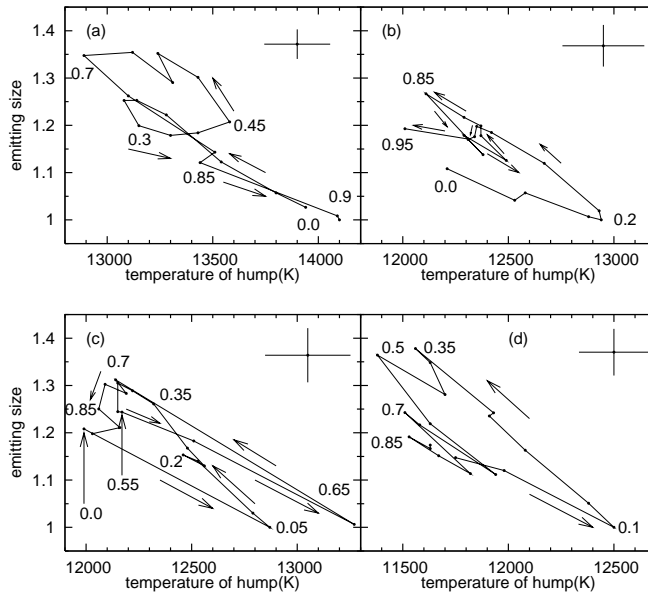


Fig. 10. Temporal variation of the emitting size against the temperature of the blackbody emission. The abscissa and the ordinate denote the blackbody temperature and the emitting size shown in figure 9, respectively. Typical errors of each point are shown at the upper-right corner of each panel. Panels (a), (b), (c), and (d) represent the results at $T = 5$, 7, 8, and 14, respectively. The numbers represent the hump phase.

analyzed the SEDs with a model including a non-variable component and discuss in this section how it changes the results.

We consider that the observed flux is a sum of the flux from the hump and the non-variable components. The SEDs of both components were assumed to be reproduced by the combination model of blackbody and 10^5 K free-free emission, as used in the last sections. We could not, however, significantly determine all parameters of both components using the 6-band photometric data. We, hence, make further assumptions for the SED model of the non-variable component. The flux ratio of the hump to the non-variable components is, in particular, difficult to be determined. The most simple way is to define the flux of the non-variable component as the observed flux at the hump minimum. The left panel of figure 11 shows the observed SEDs at the g' -band hump minimum at $T = 5$. The long dashed line indicates the best-fitted model. If we assume the SED defined by this long dashed line to be a non-variable component, it means that the flux contribution from the hump source is 0 % at the hump minimum. It is, however, possible that the hump source had a significant contribution to the observed flux even at the hump minimum. The long dashed line in the left panel of figure 11 is, thereby, the possible upper-limit of the flux from the non-variable component. In the figure, we also show the model with 80% and 40% of the flux of the best-fitted model at the hump minimum, as indicated by

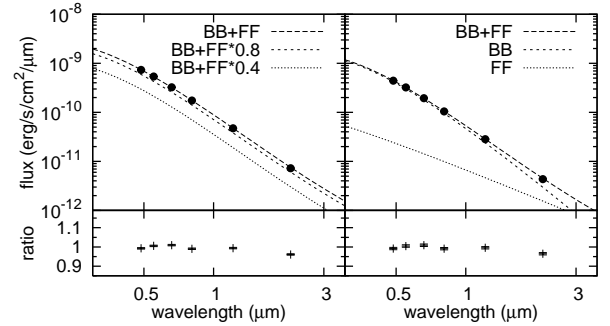


Fig. 11. Example of the SEDs of the total flux and the hump component at $T = 5$ at the g' -band hump minimum. In the left panel, the filled circles show the observed SED. The long dashed, short dashed, and dotted lines denote the best-fitted model for the observed SED, 80 % and 40 % of the flux of the best-fitted model, respectively. The latter two models were used as the non-variable component in § 4.1 (for detail, see the text). The right panel shows the SED of the hump component in the case that the non-variable component is the 40 % model. The long dashed, short dashed, and dotted lines denote the best-fitted model, its blackbody and free-free components, respectively. In the upper frames of each panel, the abscissa and ordinate denote the wavelength and flux, respectively. The errors of each point are smaller than the symbols. The lower frames show the ratio of the observed flux to the model.

the short dashed and the dotted lines. We used the 80 and 40 % models as the non-variable component in our analysis. The right panel of figure 11 shows the SED of the hump component calculated by the subtraction of the SED of the non-variable component (the 40 % model; the dotted line in the left panel) from the observed SED. As can be seen from the figure, the model well reproduces the SED of the hump component. Under those assumptions, we finally obtained the temperature and the emitting size of the blackbody emission region of the hump component.

Figure 12 shows the temporal variation of the model parameters of the blackbody emission for the hump component. The top, middle, and bottom panels show the same as figure 9. The filled squares, circles and triangles in the middle and bottom panels represent the results in the case that the non-variable component contributes 0%, 40%, and 80% of the flux at the g' -band hump minimum, respectively. The result from the 0 % model corresponds to that reported in subsection 3.4. The left and right panels show the results of the early superhump at $T = 5$ and the ordinary superhump at $T = 14$, respectively.

In the case that the contribution of the non-variable component is large, the variation amplitudes of the parameters are large. This can naturally be understood because the observed SED variation must be reproduced by the flux from a small contribution of the hump component. Except for the variation amplitude, the temporal behaviors of the parameters are qualitatively almost the same in all cases, independent of the contribution of the non-variable component.

The size of the blackbody emission expands > 3 times from the hump minimum in the case of the 80 % contri-

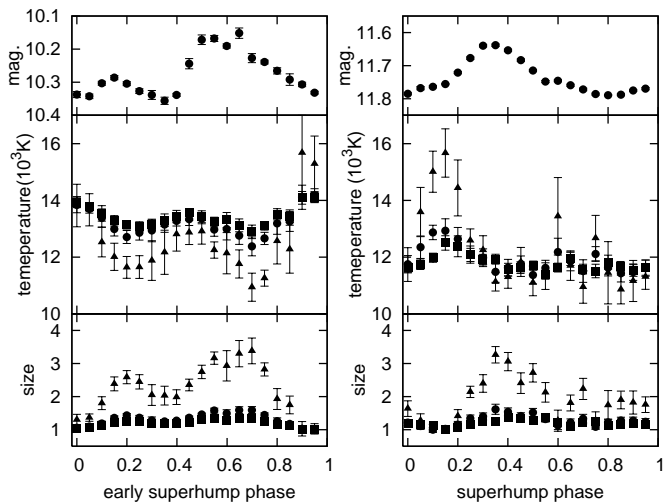


Fig. 12. Temporal variation of the temperature and the size of the blackbody emission region from the hump component. The abscissa represents the phase of the humps. The top panels show the observed V -band light curve. The middle and bottom panels show the estimated temperature and the size of the emitting region. The filled squares, circles and triangles represent the results in the case that the non-variable component contributes 0%, 40%, and 80% of flux at the g' -band hump minimum, respectively. The left and right panels show the results at $T = 5$ and $T = 14$, respectively. The size of emitting region is normalized at the minimum value.

tribution model both in the early and ordinary superhumps. Early superhumps are proposed to be variations caused by the vertical deformation in the disk (Kato 2002). In this case, we can estimate the height, h , at the outermost region of the disk which is required to explain the > 3 times expansion of the apparent emitting area. We consider that we see a flat part ($h = 0$) of the disk at an inclination angle of 75° at the hump minimum and a vertically-expanded part at the hump maximum (Araujo-Betancor et al. 2005). We calculated the height to be $h > 1.1r$ at the hump maximum where r is a disk radius. This height is, however, too large to be explained within the framework of the standard accretion disk model ($h \sim 0.1r$; Shakura, Syunyaev 1973). The 0% contribution model yields $h \sim 0.18r$, which is still slightly larger than that expected from the standard model. These results indicate that the contribution of the non-variable component in the inner disk should be small in the optical-infrared regime. In other words, the hump source significantly contributes even at the hump minimum.

4.2. Implication of the Remnant Hot Disk in Echo Outbursts

Some WZ Sge-type dwarf novae experienced echo outbursts after the main superoutburst (Kato et al. 2004). The echo outburst can be triggered if a substantial amount of gas is left at the outermost part of the disk even after the main outburst and works as a mass reservoir (Kato et al. 1998; Kato et al. 2004; Hellier 2001; Osaki et al.

2001).

V455 And showed no echo outburst, while our analysis revealed an intriguing feature just after the superoutburst. As reported in subsection 3.2, the blackbody emission remained at a moderately high temperature for 10–20 days after the superoutburst. That period corresponds to the period in which echo outbursts are observed in the other WZ Sge stars. The strong contribution of the blackbody emission indicates the presence of a luminous accretion disk, in other words, a substantial amount of the gas remains even after the outburst. The remnant disk with the moderately high temperature can, therefore, be a sign of the expected mass reservoir. V455 And showed no echo outburst, possibly because the amount of the remnant gas was not enough to trigger an echo outburst.

Hameury et al. (2000) suggests that an echo outburst is caused by an enhanced mass-transfer rate from the secondary. In this case, we can expect a high luminosity of the hot spot just after the outburst, and hence a high contribution of the free-free emission from the hot spot to the observed SED. The contribution from the hot spot should then decrease after the echo outburst phase. Figure 4 indicates that the contribution of the free-free emission keeps a gradual increase for $T = 0$ –40, and then becomes saturated after $T \sim 40$, without showing the decrease as expected from the enhanced mass-transfer scenario. Thus, no sign of the enhanced mass-transfer rate was confirmed in our data.

After $T \sim 40$, the temperature and the size of the blackbody emission region remains constant. Araujo-Betancor et al. (2005) estimates that the surface temperature of the white dwarf in V455 And is ~ 10500 K at quiescence, which is close to the estimated temperature after $T \sim 40$. We propose that the blackbody emission after $T \sim 40$ originated from the white dwarf, which becomes a dominant source in the blue part of the SED due to a weakening of the disk emission.

4.3. The Origin of the Early Superhump

Our SED analysis showed that the early superhump light source is an expanded low-temperature component. The site and the direction of the expansion are, however, unclear only in our analysis. Early superhumps are considered to be caused by a rotational effect of the accretion disk in which a part of the disk vertically expands (Kato 2002). According to the standard disk model, the temperature of the disk is lower in an outer region. Our result in subsection 3.4, hence, indicates that a part of the outer region in the disk is vertically expanded. The vertical expansion may be caused by scenarios proposed by Kato (2002) and Osaki, Meyer (2002). These models need to be re-examined to explain the color behavior associated with the early superhumps of V455 And which were observed for the first time in WZ Sge stars.

4.4. Temperature of Superhump: Observations and Theories

In subsections 3.4 and 4.1, we reported the temperature variation associated with the superhumps. There have

been only few observations that provide the superhump temperature based on multi-band photometry. Hassall (1985) observed the superoutburst of EK TrA, and reported that the superhump light-source has a temperature of ~ 5700 K. The color at the superhump maximum was redder than that at the hump minimum. Naylor et al. (1987) reported a similar result for OY Car, proposing a superhump temperature of ~ 8000 K. Smak (2005), however, theoretically predicted that the superhump temperature should be quite high in order to reproduce the observed superhump amplitude. The superhump temperature is then predicted to be > 15000 K. In this case, the color at the hump maximum should be bluer than that at the minimum.

Our observation showed that the object reached the hump maximum after the heating phase ended, and the subsequent expansion started. Smak (2005) only discuss the heating phase of superhumps. The temperature at the hump maximum can, however, be lower than that at the temperature maximum. The apparently low-temperature superhumps reported in Hassall (1985) and Naylor et al. (1987) can be explained by a strong contribution of the expanded low-temperature region. In Smak (2005), an estimation of the temperature at the superhump light source was performed with a superhump amplitude of 0.2–0.3 mag. In the case of V455 And, the amplitude of the hump was so small (~ 0.03 mag) during the heating phase that the superhump light source could avoid to take a quite high temperature. The discrepancy between the observed and theoretically expected temperatures can thus be reconciled in our results.

We note, however, that the color behavior associated with superhumps has not been established. As also commented in Smak (2005), there are several reports that systems become bluest at the superhump maximum (Schoembs, Vogt 1980; Stolz, Schoembs 1984). Such results are inconsistent with the observed color behavior in V455 And. It is possible that WZ Sge stars have a different structure of the superhump light source compared with ordinary SU UMa stars. Thus, it is premature to conclude that the color behavior observed in V455 And is common to all SU UMa stars.

5. Summary

We performed photometric observations of the 2007 superoutburst of V455 And. Our 6-band simultaneous observations allowed us to investigate the temporal variation of the temperature and the size of the emitting region associated with the superoutburst, early, and ordinary superhumps. We summarize our findings below.

- The optical emission was dominated by blackbody radiation from the accretion disk during the superoutburst, while small excesses were found in the observed flux in the near-infrared region.
- V455 And showed no echo outburst after the superoutburst. The temperature of the accretion disk rapidly declined at the same time when the object

entered a rapid fading phase. The temperature decline then stopped at ~ 8000 K. The size of the emitting region, on the other hand, kept a gradual decline. It indicates that the optically thick disk remained at a moderately high temperature even after the superoutburst. We propose that it is a sign of a mass reservoir that can trigger echo outbursts.

- A heating and a subsequent expansion-cooling processes were associated with the rising phase of superhumps. The temperature maximum preceded the superhump maximum. It indicates that the object reached the superhump maximum by the expansion of a low temperature region after the heating phase ended.
- In a cycle of early superhumps, the object was bluest at the hump minimum. This indicates that the temperature of the early superhump light source is lower than that of an underlying component. The early superhump light source is probably a low-temperature, vertically expanded region at the outermost part of the disk.

I would like to thank T.Kato and H.Maehara for their valuable comments on this paper. This work was partly supported by a Grant-in-Aid from the Ministry of Education, Culture, Sports, Science, and Technology of Japan (19740104).

References

- Araujo-Betancor, S., Gänsicke, B. T., Hagen, H.-J., Marsh, T. R., Harlaftis, E. T., Thorstensen, J., Fried, R. E., Schmeer, P., & Engels, D. 2005, *A&A*, 430, 629
- Araujo-Betancor, S., Gänsicke, B. T., Hagen, H.-J., Marsh, T. R., Thorstensen, J., Harlaftis, E. T., Fried, R. E., & Engels, D. 2004, in *Revista Mexicana de Astronomia y Astrofisica Conference Series*, ed. G. Tovmassian, & E. Sion Vol. 20 of *Revista Mexicana de Astronomia y Astrofisica*, vol. 27, 190
- Clarke, J. T., Bowyer, S., & Capel, D. 1984, *ApJ*, 287, 845
- Hōshi, R. 1979, *Progress of Theoretical Physics*, 61, 1307
- Hameury, J.-M., Lasota, J.-P., & Warner, B. 2000, *A&A*, 353, 244
- Hassall, B. J. M. 1985, *MNRAS*, 216, 335
- Hellier, C. 2001, *PASP*, 113, 469
- Horne, K., La Dous, C. A., & Shafter, A. W. 1990, in 11. North American Workshop on Cataclysmic Variables and Low-Mass X-Ray Binaries, 109
- Kato, T. 2002, *PASJ*, 54, L11
- Kato, T., Maehara, H., & Monard, B. 2008, *PASJ*, 60, L23
- Kato, T., Nogami, D., Baba, H., & Matsumoto, K. 1998, in *Wild Stars in the Old West*, ASP Conf. Ser. 137, ed. S. Howell, E. Kuulkers, & C. Woodward (PublisherASP), 9
- Kato, T., Nogami, D., Baba, H., Matsumoto, K., Arimoto, J., Tanabe, K., & Ishikawa, K. 1996, *PASJ*, 48, L21
- Kato, T., Nogami, D., Matsumoto, K., & Baba, H. 2004, *PASJ*, 56, 109
- Kato, T., Sekine, Y., & Hirata, R. 2001, *PASJ*, 53, 1191
- Kunze, S. & Speith, R. 2005, in *The Astrophysics of Cataclysmic Variables and Related Objects*, ed. J.-M. Hameury, & J.-P. Lasota Vol. 330 of *Astronomical Society of the Pacific Conference Series*, 389

- Naylor, T., Charles, P. A., Hassall, B. J. M., Bath, G. T., Berriman, G., Warner, B., Bailey, J., & Reinsch, K. 1987, *MNRAS*, 229, 183
- Nogami, D., Hiroi, K., Suzuki, Y., Moritani, Y., Soejima, Y., Imada, A., Hashimoto, O., Kinugasa, K., et al. 2009, in *ASP Conf. Ser.*, The 8th Pacific Rim Conference on Stellar Astrophysics, ed. B. Soonthornthum, S. Komonjinda, K. S. Cheng, & K. Leung (San Francisco: ASP), in press.
- O'Donoghue, D., Chen, A., Marang, F., Mittaz, J. P. D., Winkler, H., & Warner, B. 1991, *MNRAS*, 250, 363
- Osaki, Y. 1989, *PASJ*, 41, 1005
- Osaki, Y. 1995, *PASJ*, 47, 47
- Osaki, Y. 1996, *PASP*, 108, 39
- Osaki, Y. & Meyer, F. 2002, *A&A*, 383, 574
- Osaki, Y., Meyer, F., & Meyer-Hofmeister, E. 2001, *A&A*, 370, 488
- Patterson, J., Masi, G., Richmond, M. W., Martin, B., Beshore, E., Skillman, D. R., Kemp, J., Vanmunster, T., et al. 2002, *PASP*, 114, 721
- Patterson, J., McGraw, J. T., Coleman, L., & Africano, J. L. 1981, *ApJ*, 248, 1067
- Schlegel, D. J., Finkbeiner, D. P., & Davis, M. 1998, *ApJ*, 500, 525
- Schoembs, R. & Vogt, N. 1980, *A&A*, 91, 25
- Shakura, N. I. & Syunyaev, R. A. 1973, *A&A*, 24, 337
- Skrutskie, M. F., Cutri, R. M., Stiening, R., Weinberg, M. D., Schneider, S., Carpenter, J. M., Beichman, C., Capps, R., et al. 2006, *AJ*, 131, 1163
- Smak, J. 2005, *Acta Astronomica*, 55, 367
- Smak, J. I. 1993, *Acta Astronomica*, 43, 101
- Smith, J. A., Tucker, D. L., Kent, S., Richmond, M. W., Fukugita, M., Ichikawa, T., Ichikawa, S., Jorgensen, A. M., et al. 2002, *AJ*, 123, 2121
- Stolz, B. & Schoembs, R. 1984, *A&A*, 132, 187
- Szkody, P. 1976, *ApJ*, 207, 824
- Uemura, M., Arai, A., Krajci, T., Pavlenko, E., Shugarov, S. Y., Katysheva, N. A., Goranskij, V. P., Maehara, H., et al. 2008, *PASJ*, 60, 227
- Warner, B. 1985, in *Interacting Binaries*, ed. P. P. Eggleton, & J. E. Pringle (PublisherReidel), 367
- Warner, B. 1995, *Cataclysmic Variable Stars* (Cambridge University Press)
- Warner, B. & O'Donoghue, D. 1988, *MNRAS*, 233, 705
- Watanabe, M., Nakaya, H., Yamamuro, T., Zenno, T., Ishii, M., Okada, M., Yamazaki, A., Yamanaka, Y., et al. 2005, *PASP*, 117, 870
- Whitehurst, R. 1988, *MNRAS*, 232, 35